

RESEARCH ARTICLE

The role of cloud phase in Earth's radiation budget

10.1002/2016JD025951

Key Points:

- Cloud phase partitioning plays a significant role in the global energy budget
- Global impacts of liquid, ice, and mixed-phase clouds are assessed using CloudSat's multisensor radiative fluxes product
- Results highlight the importance of mixed-phase clouds in influencing global heat transport

Correspondence to:

A. V. Matus,
amatus@wisc.edu

Citation:

Matus, A. V. and T. S. L'Ecuyer (2017), The role of cloud phase in Earth's radiation budget, *J. Geophys. Res. Atmos.*, 122, doi:10.1002/2016JD025951.

Received 28 SEP 2016

Accepted 6 FEB 2017

Accepted article online 10 FEB 2017

Alexander V. Matus¹ and Tristan S. L'Ecuyer¹¹Department of Atmospheric and Oceanic Sciences, University of Wisconsin-Madison, Madison, Wisconsin, USA

Abstract The radiative impact of clouds strongly depends on their partitioning between liquid and ice phases. Until recently, however, it has been challenging to unambiguously discriminate cloud phase in a number of important global regimes. CloudSat and CALIPSO supply vertically resolved measurements necessary to identify clouds composed of both liquid and ice that are not easily detected using conventional passive sensors. The capability of these active sensors to discriminate cloud phase has been incorporated into the fifth generation of CloudSat's 2B-FLXHR-LIDAR algorithm. Comparisons with Clouds and the Earth's Radiant Energy System fluxes at the top of atmosphere reveal that an improved representation of cloud phase leads to better agreement compared to earlier versions of the algorithm. The RMS differences in annual mean outgoing longwave (LW) radiation gridded at 2.5° resolution are 4.9 W m⁻², while RMS differences in outgoing shortwave (SW) are slightly larger at 8.9 W m⁻² due to the larger diurnal range of solar insolation. This study documents the relative contributions of clouds composed of only liquid, only ice, and a combination of both phases to global and regional radiation budgets. It is found that mixed-phase clouds exert a global net cloud radiative effect of -3.4 W m⁻², with contributions of -8.1 W m⁻² and 4.7 W m⁻² from SW and LW radiation, respectively. When compared with the effects of warm liquid clouds (-11.8 W m⁻²), ice clouds (3.5 W m⁻²), and multilayered clouds consisting of distinct liquid and ice layers (-4.6 W m⁻²), these results reinforce the notion that accurate representation of mixed-phase clouds is essential for quantifying cloud feedbacks in future climate scenarios.

1. Introduction

Water in Earth's atmosphere exists in all three thermodynamic phases—liquid, ice, and vapor—with each phase playing a unique role in Earth's radiation budget. While the radiative effects of water vapor are fairly well understood [Soden and Held, 2006], clouds continue to represent a significant source of uncertainty in our ability to understand present-day energy flows and predict future climate [Randall et al., 2007; Flato et al., 2013]. Beyond the need to accurately represent the global distribution of clouds, the radiative effects of clouds on shortwave (SW) and longwave (LW) radiation strongly depend on the cloud phase [Slingo, 1989; Fu and Liou, 1993]. Clouds that form at temperatures warmer than 0°C can be assumed to contain only liquid droplets, while those found at temperatures colder than -40°C are generally composed entirely of ice crystals [Pruppacher et al., 1998]. At temperatures between -40°C and 0°C, however, clouds may consist entirely of ice crystals, supercooled liquid water droplets, or a mixture of both (known as mixed-phase clouds), complicating estimates of their radiative effects. Simply changing liquid to ice near cloud top can, in turn, dramatically alter cloud albedo and lead to large differences in a cloud's impact on its environment [Forbes and Ahlgrim, 2014; Kay et al., 2016].

Given their expansive coverage and wide range of radiative properties, mixed-phase clouds impact climate on a global scale. The presence of supercooled liquid in mixed-phase clouds is especially important since liquid water is more opaque to longwave radiation and increases cloud albedo more than ice crystals [Hogan et al., 2003]. Supercooled liquid water has been observed globally in the atmosphere [Hogan et al., 2004; Verlinde et al., 2007; Hu et al., 2010] and, in particular, at higher latitudes where it is a significant driver of radiative fluxes [Cesana et al., 2012; van Tricht et al., 2016]. Despite their importance in the global energy budget, however, it has been shown that supercooled liquid water clouds are often underestimated in global climate models (GCMs) [Komurcu et al., 2014; Cesana et al., 2015; McIlhatten et al., 2017]. Furthermore, mixed-phase clouds may have an even greater role in a future climate as increasing greenhouse gas concentrations are expected to change not only the spatial coverage of mixed-phase clouds but also their ice-liquid partitioning [Komurcu et al., 2014]. An increase in cloud optical depth poleward of 45° appears to be a robust response to warming

in GCMs and has been attributed to a transition from ice-dominated to liquid-dominated mixed-phase clouds [Tsushima *et al.*, 2006; Zelinka *et al.*, 2013; Komurcu *et al.*, 2014; Mccoy *et al.*, 2015]. Given the sensitivity of GCMs to cloud water phase, a more realistic representation of phase partitioning is critical for establishing confidence in such cloud feedback estimates in future climate simulations.

Mixed-phase clouds are often crudely represented in global models that oversimplify the complex microphysical processes that influence transitions between liquid and ice [Prenni *et al.*, 2007]. Phase transition mechanisms including nucleation, secondary ice formation, and the Bergeron-Findeisen process remain poorly represented as a result [Atkinson *et al.*, 2013; Murray *et al.*, 2013; Cesana *et al.*, 2015]. Constraining these phase transition mechanisms is particularly challenging since the physics and dynamics of mixed-phase clouds are nonlinear [Morrison *et al.*, 2011]. Mccoy *et al.* [2015] showed that 19 models from the Coupled Model Intercomparison Project phase 5 are effectively partitioning ice and liquid as a monotonic function of temperature, which is found to contribute a substantial amount of variance in cloud fraction and liquid water path (LWP) in models. Such oversimplifications in cloud-phase partitioning can lead to significant errors when calculating cloud radiative effects in a climate model [Gettelman *et al.*, 2007; Storelmo *et al.*, 2008]. The role of low cloud feedback over the Southern Ocean, for example, is a significant source of bias and disagreement among GCMs [Bony *et al.*, 2006; Vial *et al.*, 2013]. Despite the climatic importance of clouds over this region, local observations are sparse and infrequent which limits the information available for evaluating and improving model parameterizations.

In fact, our understanding of the global impacts of mixed-phase clouds in general is limited due to sparse observations. Research aircraft and ship-based instrumentation can measure supercooled droplets on regional scales but fail to adequately characterize their microphysical properties on global scales. Satellite-based remote sensing methods provide the necessary coverage for continuous monitoring of mixed-phase clouds on larger scales [Miller *et al.*, 2014]. Since supercooled liquid tends to reside near cloud top, there is a distinct advantage to viewing mixed-phase clouds from above using satellite [Raubert and Tokay, 1991]. However, while conventional passive sensors provide information about the presence of liquid water near cloud top, they lack information about cloud composition below this liquid layer in optically thick or multilayered clouds. Recent studies investigating the global radiative effects of mixed-phase clouds have noted that this failure to observe the vertical distribution of cloud optical properties remains one of the largest uncertainties in quantifying cloud radiative effects on global scales [Randall *et al.*, 2007; Hogan *et al.*, 2004; Hu *et al.*, 2010].

This study seeks to address these limitations by leveraging actively sensed cloud profile data from CloudSat and the Cloud-Aerosol Lidar and Infrared Pathfinder Satellite Observation (CALIPSO) in combination with the Moderate Resolution Imaging Spectroradiometer (MODIS). Section 2 describes updates in the new release of the CloudSat level 2 radiative fluxes and heating rates algorithm (2B-FLXHR-LIDAR) that include an improved representation of supercooled liquid water clouds, thin ice clouds, and surface albedo. In section 3, 2B-FLXHR-LIDAR performance is evaluated using collocated SW and LW flux observations from the Clouds and the Earth's Radiant Energy System (CERES) [Kato *et al.*, 2010]. Flux estimates from 2B-FLXHR-LIDAR are then used to investigate the radiative impacts of clouds over the pre-anomaly phase of the CloudSat mission (2007–2010). This time period has been selected since, after the April 2011 battery anomaly, only daytime observations are available, and the alignment of CloudSat and CALIPSO footprints is slightly degraded. Section 4 quantifies global cloud radiative effects and the relative contributions from liquid, ice, or mixed-phase clouds. Mixed-phase cloud radiative effects, in particular, are highlighted in section 5 which documents the seasonal and regional patterns of mixed-phase clouds and assesses their implications for global heat transport. A discussion of key points from this paper is provided in section 6.

2. The Fifth Release CloudSat Fluxes and Heating Rates Data Set

The 2B-FLXHR-LIDAR algorithm estimates vertically resolved fluxes and heating rates consistent with retrieved cloud properties from CloudSat, CALIPSO, and MODIS [L'Ecuyer *et al.*, 2008; Henderson *et al.*, 2013]. Algorithm inputs include CloudSat retrievals of liquid and ice water contents and effective radii, temperature and humidity profiles from European Centre for Medium-Range Weather Forecasts analyses, and seasonally varying surface albedo and emissivities using land surface classification data provided by the International Geosphere-Biosphere Programme. Snow and ice cover are identified using collocated passive microwave observations from Advanced Microwave Scanning Radiometer–EOS provided by the National Snow and Ice Data Center. These inputs initialize broadband radiative flux calculations in a two-stream, plane-parallel,

adding-doubling radiative transfer model [Ritter and Geleyn, 1992] to compute fluxes in 6 shortwave and 12 longwave bands. Resulting fluxes are output for each CloudSat footprint at a vertical resolution of 240 m.

The fifth release (R05) 2B-FLXHR-LIDAR data set makes several significant advances over the previous version (R04) described in Henderson *et al.* [2013, hereafter H13]. The new algorithm features improved land, snow, and sea ice albedos using spectral measurements from Zatko and Warren [2015], a more realistic representation of the zenith angle dependence of ocean albedo, an explicit representation of lidar-detected supercooled liquid water clouds, and a more rigorous treatment of thin ice clouds that includes explicit retrievals of ice water content (IWC) and effective radii from the CloudSat 2C-ICE data product [Deng *et al.*, 2013]. These improvements incorporate better physical assumptions and yield better agreement relative to validation data sets. As with any remote sensing-based data set, however, a number of limitations remain including retrieval errors and sampling biases that result from the spatial and temporal sampling characteristics of CloudSat and CALIPSO. While CloudSat is more sensitive to optically thick clouds and CALIPSO is better suited at detecting optically thin clouds, it is likely that some cloud features may go undetected by both sensors. CALIPSO may fail to detect very thin liquid layers ($LWP < 5 \text{ g m}^{-2}$) and may miss layers in clouds below optically thick ice layers above [Christensen *et al.*, 2013]. Since CALIPSO lidar may be attenuated by optically thick supercooled liquid layers which prevents the detection of underlying ice layers, CALIPSO may miss mixed-phase clouds over polar regions where supercooled-topped mixed-phase clouds are common [Morrison *et al.*, 2011; Cesana *et al.*, 2012]. The influence of these uncertainties on the results will be evaluated through a combination of sensitivity studies and comparisons against independent top-of-atmosphere (TOA) flux data sets in section 3.

The R05 data set comprises 285 million radiative flux profiles with near-global coverage (82.5°S to 82.5°N) from July 2006 to April 2011. For quality control, profiles with incomplete or missing input data are screened using the quality control flags supplied with the product. Data are screened based on the following criteria: missing Cloud-Aerosol Lidar with Orthogonal Polarization (CALIOP) observations, missing MODIS observations, or out-of-bounds flux estimates. The specific criteria are described in greater detail in Table 14 of the CloudSat 2B-FLXHR-LIDAR Data Product Documentation [Henderson and L'Ecuyer, 2011]. Altogether, these criteria result in less than 0.3% of the data being excluded from the analysis.

3. Algorithm Performance

To evaluate the performance of the FLXHR-LIDAR flux product, estimates of SW and LW fluxes at the TOA are compared with CERES single scanner footprint (SSF) fluxes reported in the CALIPSO, CloudSat, CERES, and MODIS (C3M) product [Kato *et al.*, 2010]. The CERES instrument aboard Aqua provides a long-term, continuous data set of high-quality SW and LW fluxes. Since the Aqua satellite orbits closely with CloudSat and therefore views nearly identical atmospheric conditions, the CERES SSF product is a particularly valuable tool for validating FLXHR-LIDAR fluxes. Figure 1 compares TOA albedo in clear-sky and all-sky scenes from CERES with FLXHR-LIDAR estimates from both the R04 and R05 versions of the algorithm. It is found that the R04 version of FLXHR-LIDAR exhibits significant clear-sky biases over most land surfaces and most notably over deserts, forests, and tundra. In the new R05 version, corrections to land and ocean surface reflectances have reduced the global mean bias by over 40% in clear-sky scenes, resulting in a TOA albedo offset of just -0.7% . Regionally, these biases in clear-sky albedo have improved by as much as 20% over Greenland and Antarctic ice sheets, 10% over tropical forests, and 5% over deserts.

All-sky biases have also been reduced in R05 through the improved representation of mixed-phase clouds and thin cirrus. In particular, the positive bias over subtropical ocean has been improved from 4 W m^{-2} in R04 to 1 W m^{-2} in R05, while the negative bias over the Southern Ocean has been improved from -6 W m^{-2} to -2 W m^{-2} , primarily due to the explicit detection of supercooled liquid in the new R05 FLXHR-LIDAR algorithm. The spatial structure of albedo in R05 has improved significantly over the entire globe and especially over polar regions where much attention has been given toward better understanding the surface energy budget [Verlinde *et al.*, 2007; Christensen *et al.*, 2016]. Overall, clear-sky and all-sky albedo estimates compare favorably between CERES and R05, with global annual mean differences less than 1%.

Similar comparisons of outgoing longwave radiation (OLR) are shown in Figure 2. There are two significant changes in R05 affecting OLR: (1) updating greenhouse gas concentrations to 2010 levels and (2) including explicit retrievals of IWC and effective radius from 2C-ICE. Increasing carbon dioxide concentrations from 330 ppm in R04 to 390 ppm in R05 results in a global reduction in clear-sky OLR of -1.3 W m^{-2} . This reduction

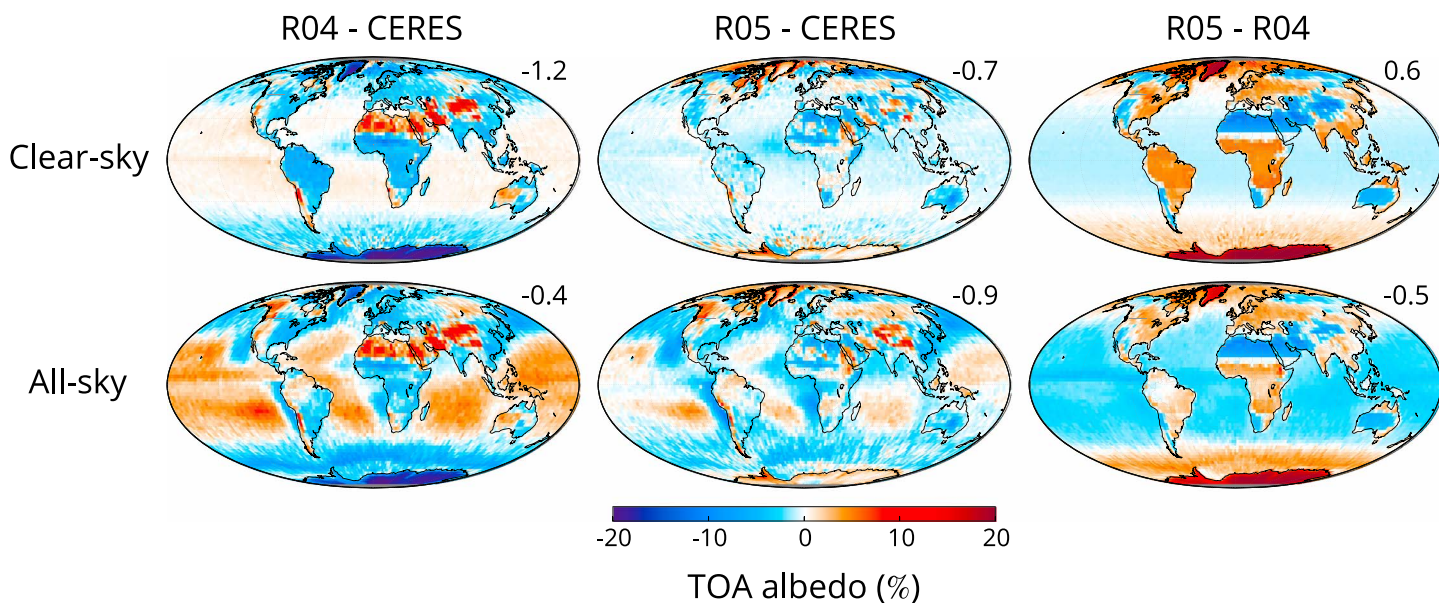


Figure 1. Comparisons of annual mean top-of-atmosphere (TOA) albedo from R05 FLXHR-LIDAR, R04 FLXHR-LIDAR, and CERES SSF over 2007–2010. Values displayed in the top right of all maps are area-weighted global averages.

in OLR helps to improve the positive bias observed at higher latitudes. The addition of 2C-ICE retrievals in R05 increases all-sky OLR over the tropics, offsetting a negative bias resulting from increased greenhouse gas concentrations in that region. While all-sky OLR biases have increased slightly to 9 W m^{-2} at higher latitudes, biases are similar to R04 elsewhere and even exhibit a slight improvement over the equatorial Pacific.

Root-mean-square (RMS) differences between annual mean fluxes at $2.5^\circ \times 2.5^\circ$ spatial resolution from FLXHR-LIDAR and CERES are shown in Figure 3. The RMS differences in clear-sky outgoing shortwave radiation (OSR) are 7.5 W m^{-2} , while those for OLR are 2.8 W m^{-2} . Higher RMS differences in SW fluxes can be attributed to the larger diurnal range in solar insolation (0 to 450 W m^{-2}) compared to that of thermal emission (200 to 450 W m^{-2}). The RMS differences for all-sky OSR and OLR are 8.9 W m^{-2} and 4.9 W m^{-2} , respectively, which improve upon R04 values of 16.5 W m^{-2} and 5.7 W m^{-2} reported in H13. The larger spread in flux values

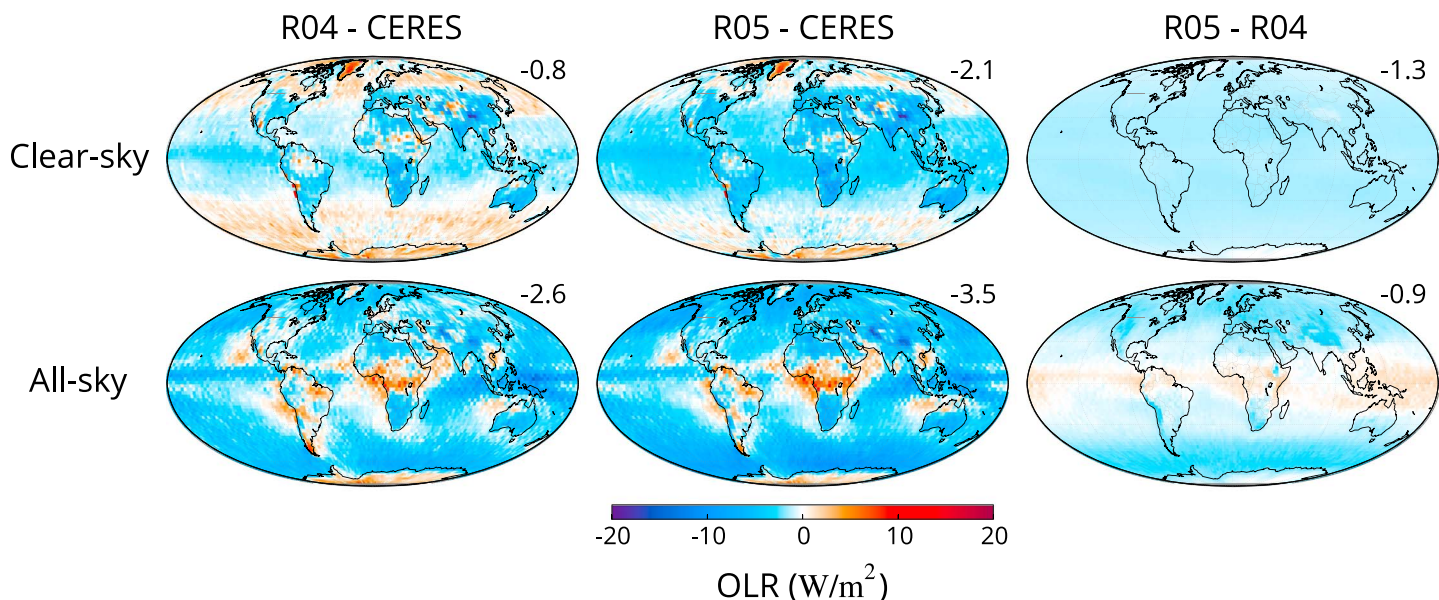


Figure 2. Same as Figure 1 but for outgoing longwave radiation (OLR).

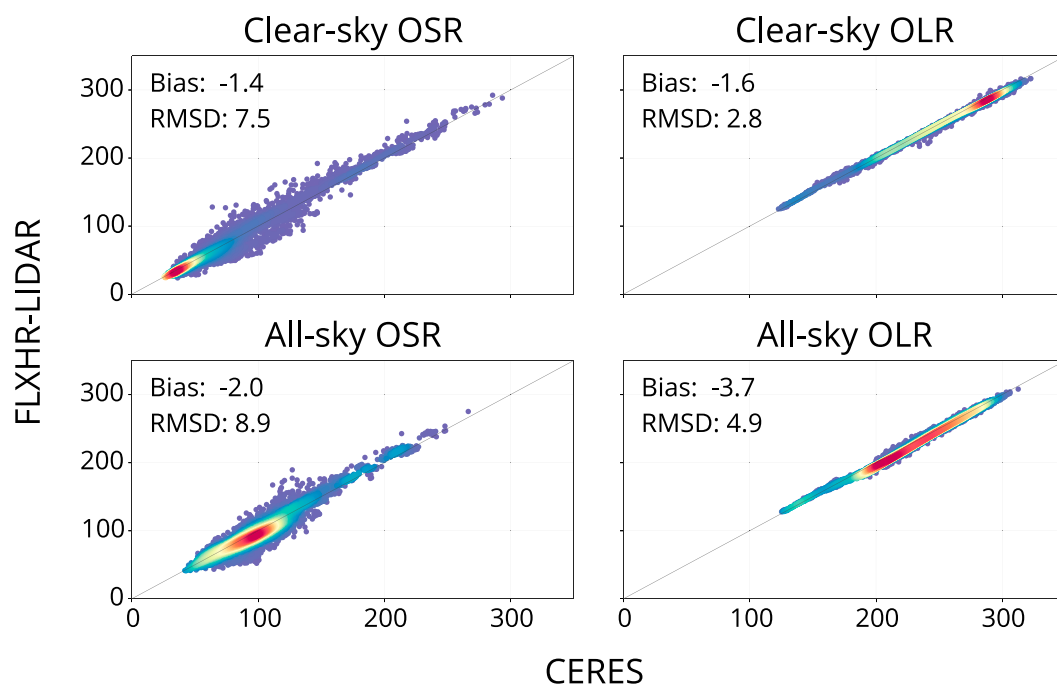


Figure 3. Scatterplots of outgoing shortwave (OSR) and longwave radiation (OLR), in W m^{-2} , comparing R05 FLXHR-LIDAR to CERES. Each point represents a $2.5^\circ \times 2.5^\circ$ latitude-longitude grid box of fluxes averaged over 2007–2010.

from all-sky scenes compared to clear-sky scenes is attributed to uncertainties in cloud microphysical property retrievals and cloud detection differences between the larger CERES and smaller CloudSat fields of view. Overall, biases in OSR and OLR are less than 4 W m^{-2} in both clear-sky and all-sky scenes. While R05 generally underestimates TOA fluxes compared to CERES, these differences are consistent with anticipated uncertainties in CERES fluxes themselves [Loeb *et al.*, 2012].

It should be noted that uncertainties in any observational quantity derived from an algorithm like FLXHR-LIDAR may vary with the time and space scales of interest. Furthermore, due to structural errors from the myriad of assumptions required in the calculations, uncertainties on every scale are a sum of random and systematic components [L'Ecuyer *et al.*, 2015]. L'Ecuyer *et al.* [2008] showed that uncertainties in fluxes derived from the original 2B-FLXHR algorithm decreased on longer time scales and this also holds true for the current 2B-FLXHR-LIDAR product. Table 1 compares fluxes from R05 relative to CERES computed over a range of time and spatial scales. While spatial averaging has a negligible impact for the range of scales considered (2.5 to 10°), the RMS differences in SW and LW fluxes decrease systematically with increasing temporal averaging as a result of reduced random errors. The RMS differences in OSR at 2.5° resolution, for example, decrease from 13.8 W m^{-2} for monthly averaging to 8.9 W m^{-2} for annual averaging. For LW fluxes, though, the change in RMSE from monthly to annual averaging is considerably less than that for SW fluxes. This highlights the importance of considering time-space scale averaging when interpreting FLXHR-LIDAR analyses of SW and LW fluxes.

While many approaches of varying complexity have been introduced for classifying clouds, we adopt an approach that simply partitions clouds according to phase. This approach not only avoids the use of subjective thresholds but also relates more directly to prognostic fields in numerical models, potentially offering a more direct means of evaluating their representation in models. The new R05 FLXHR-LIDAR algorithm features a robust cloud phase classification, improving upon previous versions that assumed a linear partitioning of liquid and ice water in cloud layers with temperatures between -20°C and 0°C [L'Ecuyer *et al.*, 2008]. The R05 FLXHR-LIDAR algorithm explicitly identifies cloud phase (liquid, ice, or mixed) in each layer of a scene using the 2B-CLDCLASS-LIDAR cloud phase classification described in Sassen and Wang [2012]. The 2B-CLDCLASS-LIDAR product combines CloudSat radar and CALIPSO lidar measurements to distinguish cloud

Table 1. The Bias and RMSE (in Parentheses) of Fluxes, in $W m^{-2}$, From R05 FLXHR-LIDAR Relative To CERES Averaged Over a Range of Time and Spatial Scales^a

Flux	Resolution	Month	Season	Year
OSR	2.5°	−2.4 (13.8)	−2.1 (11.7)	−2.0 (8.9)
	5°	−2.4 (13.6)	−2.1 (11.5)	−2.1 (8.7)
	10°	−2.4 (13.7)	−2.1 (11.7)	−2.1 (8.9)
OLR	2.5°	−3.7 (5.9)	−3.7 (5.4)	−3.7 (4.9)
	5°	−3.6 (5.9)	−3.7 (5.4)	−3.6 (4.8)
	10°	−3.6 (5.9)	−3.7 (5.3)	−3.6 (4.8)

^aNote that only observations between $\pm 80^\circ$ are included in these calculations to maintain consistency among all resolutions.

phase using signal intensity differences between liquid and ice particles. While CloudSat's Cloud Profiling Radar is particularly sensitive to cloud liquid droplets, CALIPSO's CALIOP has a greater sensitivity to smaller ice particles. Together, both radar and lidar measurements improve overall cloud detection and provide information necessary for cloud phase classification in the 2B-CLDCLASS-LIDAR product. In this study, a mixed-phase cloud refers to any contiguous cloud layer in which both liquid and ice phases are identified according to the 2B-CLDCLASS-LIDAR cloud phase classification. If more than one cloud phase is identified in multiple distinct cloud layers, then that scene is classified as a multilayered (ML) cloud system.

Table 2 summarizes comparisons of FLXHR-LIDAR and CERES fluxes categorized by scene type. Biases and RMS differences are reported as percent differences relative to CERES. Overall, clear-sky fluxes exhibit good agreement between FLXHR-LIDAR and CERES with a net bias and RMSE of less than -0.9% and 2.8% , respectively. Fluxes in cloudy scenes have slightly higher biases and spreads that can be attributed to cloud retrieval and detection differences in CERES and CloudSat/CALIPSO. In particular, the 20 km CERES scanner footprint is considerably larger than CloudSat's cross-track resolution of 1.4 km. Owing to sampling issues discussed previously, cloudy-sky fluxes exhibit better agreement in the LW than in the SW. Scenes with liquid phase clouds have a relatively low RMS of 2.2% for OLR fluxes but a higher RMS of 16.9% for OSR. This may be partially explained by differences in the fields of view of CloudSat and CERES, particularly over spatially heterogeneous clouds such as broken stratocumulus. By comparison, scenes with mixed-phase clouds have RMS differences of 8.4% and 12.7% in OLR and OSR, respectively. Given that the level of agreement in SW and LW fluxes varies by the type of cloud present in a given scene, it is important to consider the scene type when assessing the accuracy of fluxes from FLXHR-LIDAR.

Table 2. Bias and Root-Mean-Square Differences (RMSD) of Fluxes, in Percent, From FLXHR-LIDAR Relative To CERES for Scenes Containing a Given Cloud Phase (Liquid, Ice, Mixed, and Multilayered)^a

Scene Type	OSR		OLR		Net (OSR + OLR)	
	Bias	RMSD	Bias	RMSD	Bias	RMSD
Liquid phase	5.1	16.9	−1.6	2.2	0.5	4.6
Ice phase	−7.1	14.3	−2.4	4.2	−3.9	5.4
Mixed phase	7.0	12.7	−7.3	8.4	−1.2	4.3
Multilayered	0.5	9.7	−1.7	2.6	−0.9	3.2
Clear sky	−2.2	12.1	−0.6	1.1	−0.9	2.8
All sky	−2.0	8.9	−1.6	2.1	−1.8	3.2

^aCloud phase is determined based on the 2B-CLDCLASS-LIDAR cloud phase classification and includes liquid phase, ice phase, and mixed-phase clouds. Mixed-phase clouds are defined as single-layer clouds containing multiple phases, whereas multilayered (ML) clouds are assigned if CALIPSO detects cloud layers of more than one phase within a given profile.

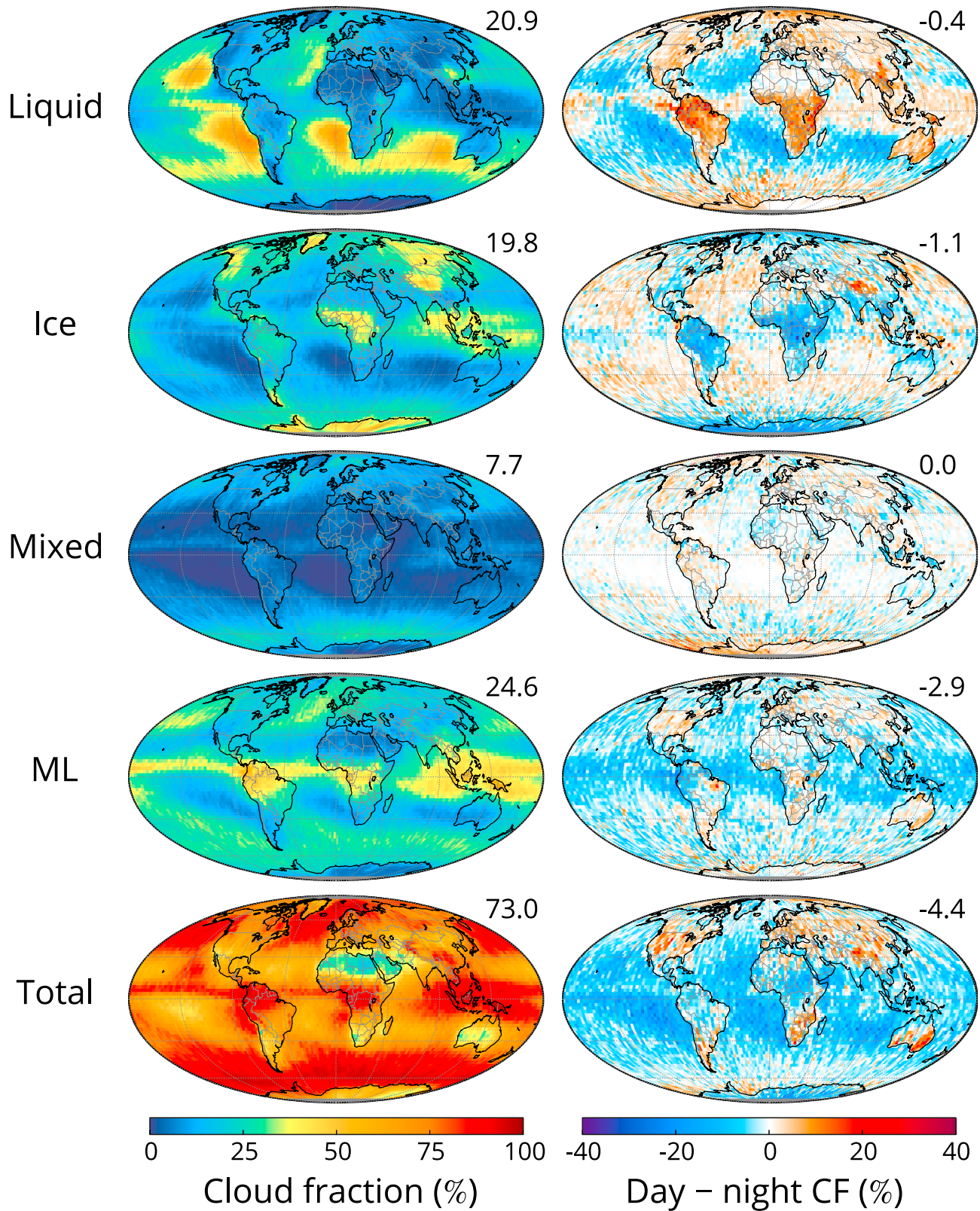


Figure 4. (left column) CloudSat/CALIPSO cloud occurrence according to water phase and (right column) the daytime minus nighttime difference in cloud occurrence. Cloud phase is determined based on the 2B-CLDCLASS-LIDAR cloud phase classification. Mixed-phase clouds are defined as single-layer clouds containing multiple phases, whereas multilayered (ML) clouds are assigned if CALIPSO detects cloud layers of more than one phase within a given profile. All data are $2.5^\circ \times 2.5^\circ$ gridded annual averages from 2007 to 2010.

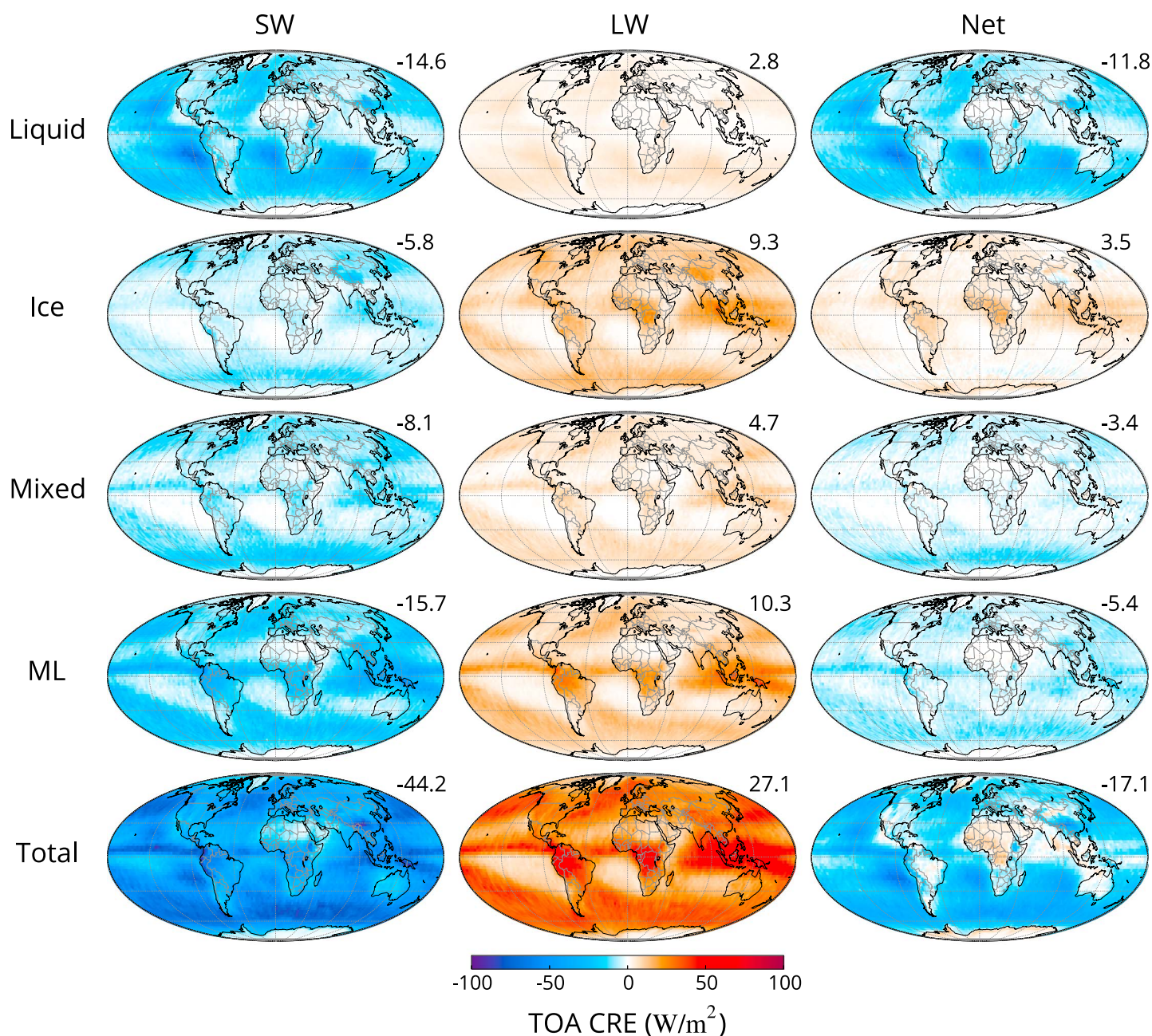


Figure 5. Annual average SW, LW, and net cloud radiative effects at the top of atmosphere (TOA). Radiative effects are separated by water phase (liquid, ice, mixed, and multilayered) using R05 FLXHR-LIDAR, 2007–2010.

4. Global Cloud Radiative Effects

The radiative impact of clouds depends not only on their geographic location but also on their composition. Figure 4 displays the annual mean frequencies of occurrence of liquid, ice, and mixed-phase clouds from CloudSat/CALIPSO observations over 2007–2010. Cloud occurrence is computed as the fractional coverage of each 2B-CLDCLASS-LIDAR cloud phase gridded at $2.5^\circ \times 2.5^\circ$ spatial resolution. A crude estimate of the diurnal variability in cloud occurrence provided in Figure 4 (right column) displays the day-night differences in cloud fraction obtained by differencing the A-Train 1:30 P.M. and 1:30 A.M. overpasses. It should be noted that CALIPSO may detect fewer weakly scattering clouds during daytime than at night due to higher solar background noise [Chepfer *et al.*, 2013], although this is not expected to affect the detection of optically thick liquid-containing clouds. While the twice-daily sampling of the A-Train does not provide complete sampling

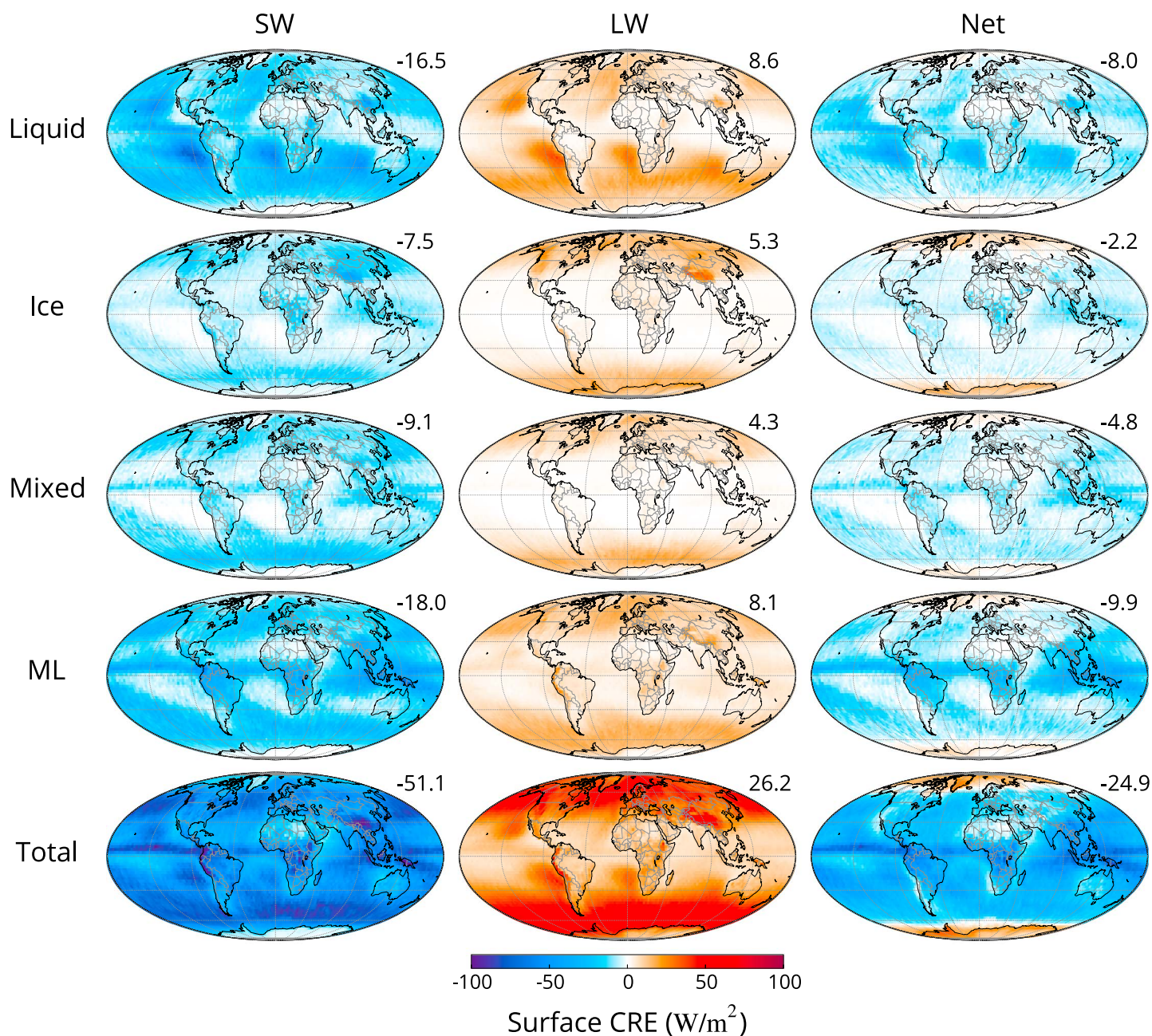


Figure 6. Same as Figure 5 but for CRE at the surface.

of diurnal variations in cloud cover, this comparison of daytime and nighttime overpasses suggests that mixed-phase clouds exhibit much weaker diurnal variations than other cloud types.

Mixed-phase clouds are considerably less common than those consisting entirely of ice or liquid water. Clouds identified as mixed-phase are observed globally in 7.7% of CloudSat/CALIPSO profiles and account for about one tenth of the total global cloud fraction of 73%. While frequently observed at higher latitudes in both hemispheres, these clouds are most prevalent over the Southern Ocean. Unlike pure liquid or ice clouds that exhibit distinct patterns of diurnal variation, mixed-phase clouds generally occur with equal frequency during daytime and nighttime overpasses. The only exception is over the Greenland and Antarctic ice sheets where mixed-phase clouds are observed twice as frequently during the day than at night. This result, however, is due to the extreme temperature differences between day and night in the Arctic, where the Sun is present for

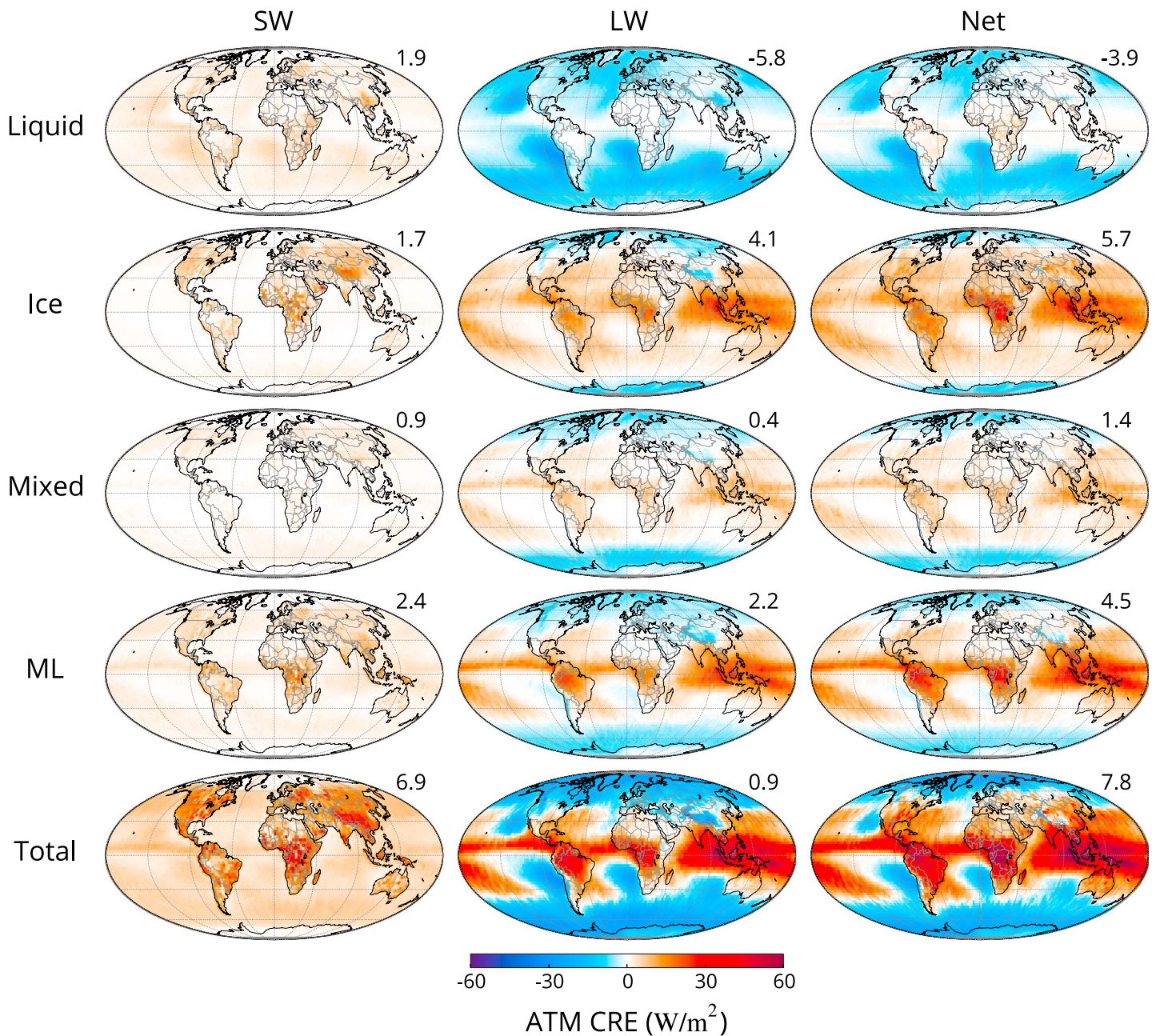


Figure 7. Same as Figure 5 but for cloud radiative effects in the atmosphere (ATM), defined as the difference between TOA CRE and surface CRE.

6 months in summer and absent for 6 months during polar night. At high latitudes, mixed-phase clouds are less common during winter months as colder temperatures limit the presence of supercooled liquid water.

The impact of clouds on radiative fluxes is commonly quantified in a metric known as cloud radiative effect (CRE)

$$CRE = (F^{\downarrow} - F^{\uparrow})_{\text{all sky}} - (F^{\downarrow} - F^{\uparrow})_{\text{clear sky}} \quad (1)$$

where F^{\downarrow} and F^{\uparrow} are downwelling and upwelling fluxes, respectively, and subscripts denote all-sky and clear-sky conditions. Figure 5 displays global maps of SW, LW, and net CRE at the TOA based on four years (2007–2010) of R05 FLXHR-LIDAR estimates. While it is well known that cloud phase significantly influences the radiative effects of clouds, the spatial patterns of CRE do not necessarily follow those of cloud phase. On the annual mean, clouds cool the planet by 17.1 W m^{-2} by reflecting 44.2 W m^{-2} of SW radiation and retaining

Table 3. Summary of Phase-Separated Global Mean Cloud Radiative Effects (Top) and Differences Between the Northern and Southern Hemispheres (Bottom), in $W m^{-2}$ ^a

		TOA CRE			SFC CRE			ATM CRE		
		SW	LW	Net	SW	LW	Net	SW	LW	Net
Global	Liquid	-14.6	2.8	-11.8	-16.5	8.6	-8.0	1.9	-5.8	-3.9
	Ice	-5.8	9.3	3.5	-7.5	5.3	-2.2	1.7	4.1	5.7
	Mixed	-8.1	4.7	-3.4	-9.1	4.3	-4.8	0.9	0.4	1.4
	ML	-15.7	10.3	-5.4	-18.0	8.1	-9.9	2.4	2.2	4.5
	Total	-44.2	27.1	-17.1	-51.1	26.2	-24.9	6.9	0.9	7.8
NH–SH	Liquid	7.0	-1.2	5.8	7.0	-4.5	2.5	-0.2	3.4	3.3
	Ice	-0.6	1.7	1.1	-1.9	1.1	-0.8	1.3	0.5	1.9
	Mixed	0.9	0.2	1.1	0.6	-0.6	0.1	0.3	0.7	1.0
	ML	0.5	0.3	0.8	-0.3	-0.6	-0.9	0.9	0.9	1.7
	Total	7.8	1.0	8.8	5.4	-4.5	0.9	2.4	5.5	7.8

^aBoth SW and LW effects from liquid, ice, mixed-phase, and multilayered clouds are computed at the top of atmosphere (TOA), surface (SFC), and within the atmospheric column (ATM). All data presented are from 2B-FLXHR-LIDAR, 2007–2010.

27.1 $W m^{-2}$ in the LW. These results are comparable to the CERES estimate of $-18.2 W m^{-2}$ reported in *Allan* [2011] but somewhat less negative than the $-24.2 W m^{-2}$ estimate from the International Satellite Cloud Climatology Project data sets [*Zhang et al.*, 2004]. While these differences in CRE estimates may be due to differences in detecting clouds and assigning optical properties, it should also be noted that CRE is computed as the difference between two sets of large numbers which can introduce significant uncertainty in the resulting estimates.

The strongest SW effects occur over the Intertropical Convergence Zone (ITCZ) where the greatest contributions are from multilayered cloud systems, as previously identified by *Lü et al.* [2015]. Shortwave CRE is also strong over the eastern subtropical ocean where liquid clouds reflect in excess of $-80 W m^{-2}$ on the annual mean. Longwave effects are equally strong over the ITCZ with large contributions from both multilayered and ice clouds, resulting in a near cancellation of LW and SW CRE over the tropical west Pacific, as noted previously by *Kiehl et al.* [1994]. Radiative effects in the LW are particularly strong for ice clouds over the tropics. Globally, ice clouds exert a positive net radiative effect of $3.5 W m^{-2}$, whereas liquid ($-11.8 W m^{-2}$), mixed-phase ($-3.4 W m^{-2}$), and multilayered clouds ($-5.4 W m^{-2}$) all induce net negative radiative effects. As a result, clouds exert a net cooling effect over much of the planet, except over polar ice sheets and equatorial Africa where LW heating dominates SW cooling. On the global annual mean, liquid phase clouds contribute nearly 70% of the net radiative effect and represent the single largest source of cooling in Earth’s energy budget.

Cloud effects at the surface can be stronger than those at the TOA due to the additional contribution of absorption. Figure 6 shows the global distributions of CRE at the surface (SFC) for each cloud phase. Overall, clouds reduce surface fluxes by $24.9 W m^{-2}$ on the global annual mean by reducing SW fluxes by $51.1 W m^{-2}$ and increasing LW fluxes by $26.2 W m^{-2}$. Cloud interactions with solar radiation are therefore 16% stronger at the surface than the TOA. Since clouds generally absorb less radiation in the SW than LW, the spatial patterns of SW CRE are similar at the TOA and surface. LW CRE, however, exhibits a substantially different spatial pattern at the surface. Larger radiative effects tend to be observed at higher latitudes for all cloud phases. The largest contribution to LW CRE is from liquid clouds that have a radiative impact of $8.6 W m^{-2}$ at the surface. For all cloud types, though, the negative SW effects dominate over the positive LW effects resulting in a negative net CRE at the surface.

The difference between CRE at the TOA and surface provides an estimate of the cloud impact on atmospheric (ATM) heating, representing the amount of radiative energy gained within the atmospheric column. The global distributions of ATM CRE for liquid, ice, mixed-phase, and multilayered clouds are displayed in Figure 7.

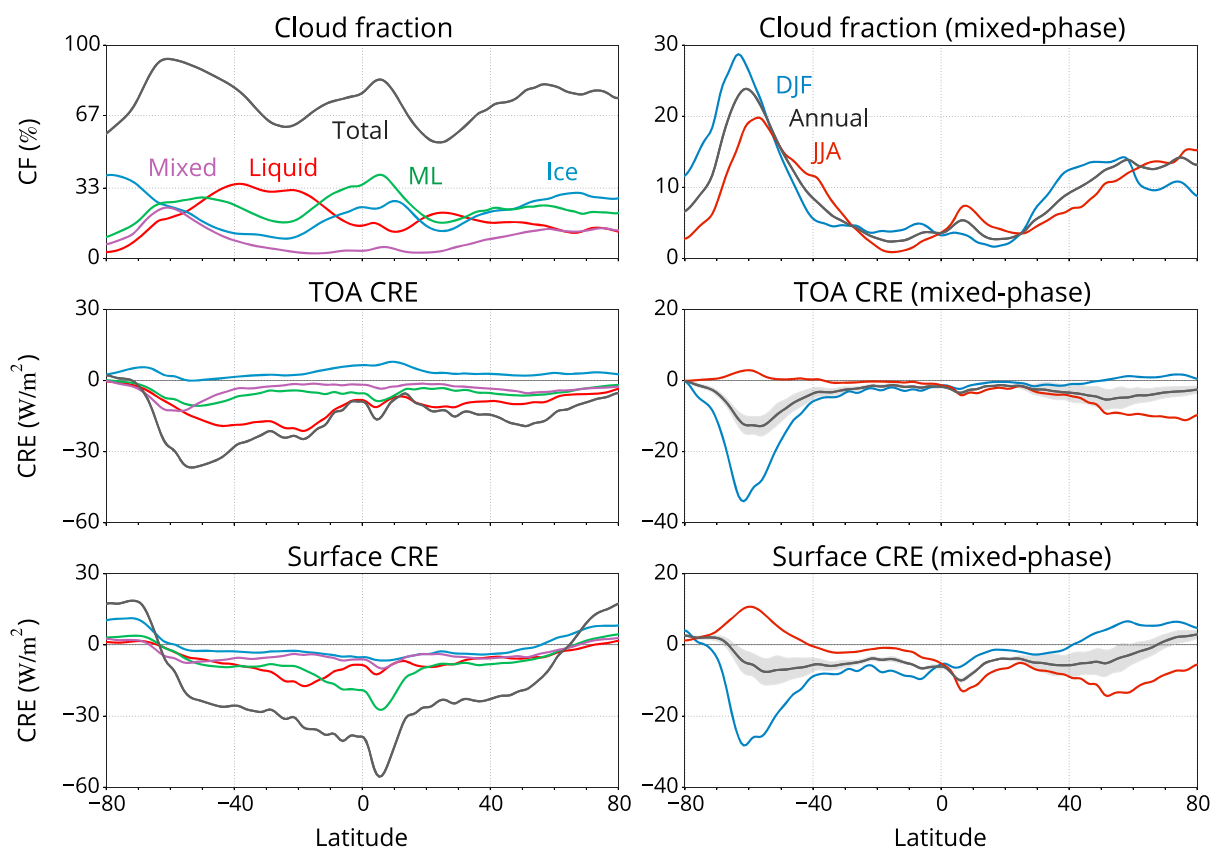


Figure 8. (top row) Zonal mean cloud fraction, (middle row) top of atmosphere cloud radiative effect, and (bottom row) surface cloud radiative effect using CloudSat/CALIPSO observations from 2007 to 2010. The left column distinguishes clouds by water phase (liquid, ice, mixed phase, and multilayered), while the right column separates mixed-phase clouds by season: December–February (DJF) and June–August (JJA). Mixed-phase clouds are defined as single-layer clouds containing multiple phases, whereas multilayered clouds are assigned to scenes with multiple discrete cloud layers of different phases. Gray shading indicates the estimated range of uncertainty in mixed-phase cloud radiative effects, computed in FLXHR-LIDAR as the flux perturbation under a scenario in which all supercooled liquid is converted to ice.

Results show that most clouds slightly enhance SW heating. Liquid and ice clouds exhibit comparable SW absorption on the global average, even though ice clouds absorb nearly exclusively over land surfaces. In the LW, liquid phase clouds exert a negative ATM CRE meaning they cool the atmospheric column. By comparison, clouds containing ice crystals tend to warm the atmosphere in equatorial regions and cool the atmosphere at higher latitudes. Overall, clouds are found to heat the atmosphere by 7.8 W m^{-2} on the global annual mean. The largest contribution to this heating is from ice clouds which contribute over 70% of the total heating.

Table 3 summarizes the FLXHR-LIDAR estimates of TOA, SFC, and ATM CRE. The upper panel documents the global mean CRE for each cloud phase, while the lower panel displays the CRE differences between Northern Hemisphere (NH) and Southern Hemisphere (SH). The most striking result is that liquid clouds exert a radiative effect at the TOA that is 7 W m^{-2} stronger in the SH owing to their higher frequency in that hemisphere. Other cloud phases exhibit negligible hemispheric differences. This implies that the observed similarity between the NH and SH radiation budgets [Wild *et al.*, 2014; Stephens and L'Ecuyer, 2015] is primarily a result of a near cancelation of the effects of increased land mass in NH and increased low cloud fraction in the SH.

5. Effects of Mixed-Phase Clouds

5.1. Global Distribution

Figure 4 shows that cloud occurrence and cloud radiative effects vary greatly by latitude. This is particularly true for mixed-phase clouds. The distribution of mixed-phase clouds and their radiative effects vary not only by region but also by season. Figure 8 presents zonal annual mean cloud fraction (top), TOA CRE (middle), and surface CRE (bottom). The left column distinguishes the relative contributions from each cloud phase (liquid, ice, mixed phase, and multilayered), while the right column displays the seasonal averages from mixed-phase

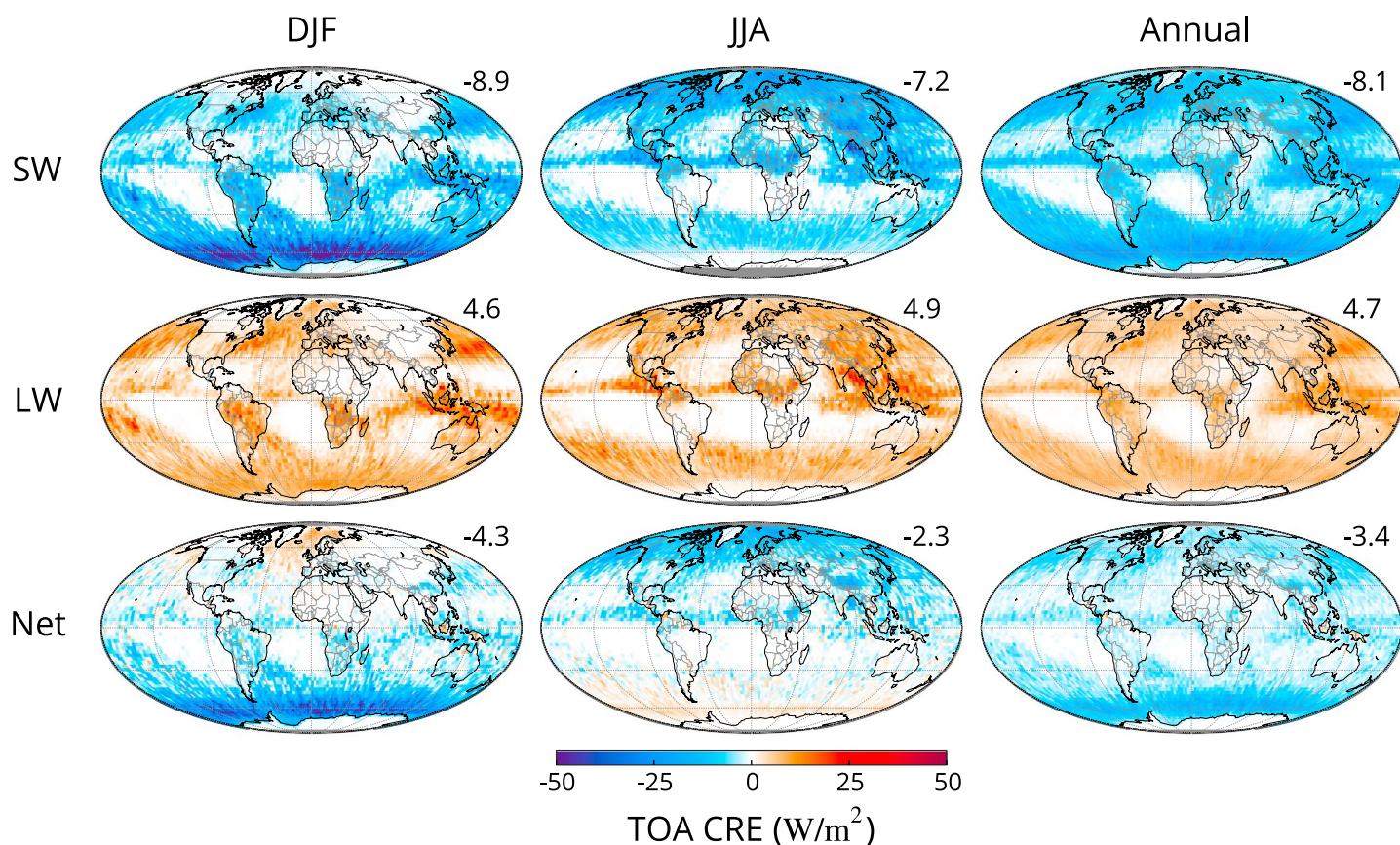


Figure 9. Seasonal and annual mean radiative effect of mixed-phase clouds at the TOA. Seasons are defined as December–February (DJF) and June–August (JJA). All data are from R05 FLXHR-LIDAR, 2007–2010.

clouds only. CloudSat/CALIPSO observations indicate that clouds are most frequently observed over the Southern Ocean around 60°S. Mixed-phase clouds are also most common in this region with an observed annual mean frequency of 23%. This region features unique cloud processes due to its relative remoteness from anthropogenic and natural continental aerosol sources [McCoy *et al.*, 2015]. During the southern hemisphere summer (December–February (DJF)) the occurrence of mixed-phase clouds exceeds 28% over the Southern Ocean and the TOA and surface CRE over this region reach peak values of -34 W m^{-2} and -28 W m^{-2} , respectively. By contrast, mixed-phase clouds over the Southern Ocean are observed less frequently during the southern hemisphere winter (June–August (JJA)) when the radiative effects at the TOA and surface are positive due to the presence of sea ice over this region. Seasonal variability is also observed in the Northern Hemisphere but to a lesser degree compared to the Southern Hemisphere.

The seasonal variability of mixed-phase cloud radiative effects is further illustrated in Figure 9, which shows the seasonal and annual mean TOA CRE of mixed-phase clouds from R05 FLXHR-LIDAR over 2007–2010. Comparable maps of CRE at the surface are displayed in Figure 10. The annual mean net TOA CRE from mixed-phase clouds is -3.4 W m^{-2} (-8.1 W m^{-2} from SW and 4.7 W m^{-2} from LW). The largest SW effects are observed in the summer hemisphere which strongly influences the global distribution of net CRE. In DJF, the net CRE from mixed-phase clouds exceeds -20 W m^{-2} over the Southern Ocean. However, in JJA there is a stronger signal from the Northern Hemisphere ITCZ in the LW CRE which partially offsets some of the SW CRE in the Northern Hemisphere. The net CRE from mixed-phase clouds in JJA is -2.3 W m^{-2} , as a result, which is over 40% weaker than in DJF. Over bright surfaces the greenhouse effect of mixed-phase clouds predominates over the albedo effect to yield a positive net mixed-phase CRE over the Southern Ocean.

5.2. Implications for Heat Transport

The significance of zonal and seasonal variations in mixed-phase cloud occurrence becomes evident in Table 4 that summarizes how their impacts on energy are partitioned between the atmosphere and ocean.

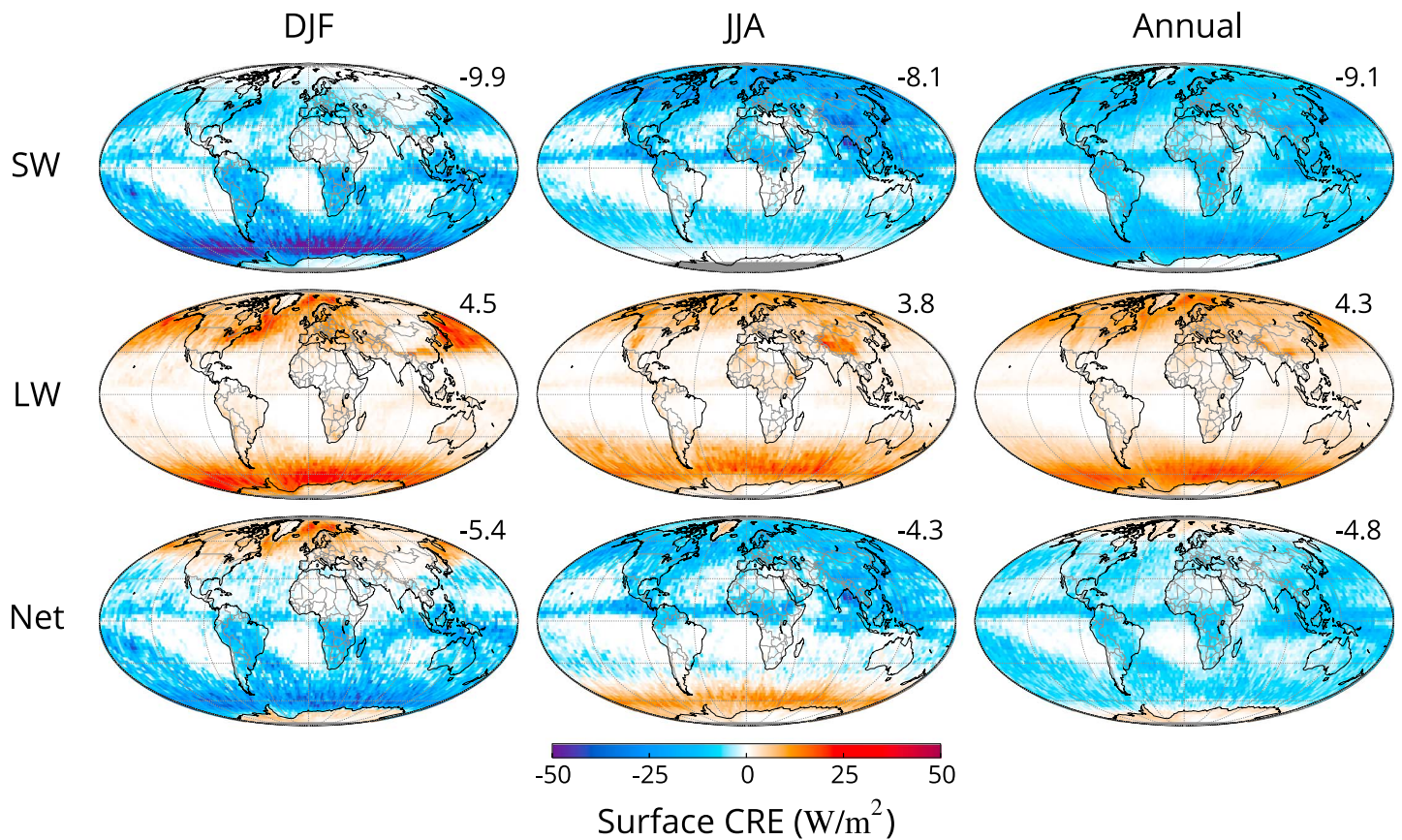


Figure 10. Same as Figure 9 but for mixed-phase CRE at the surface.

The contributions of mixed-phase clouds to net heat fluxes at the top of atmosphere, surface, and in atmosphere in each latitude zone are computed by weighting the mean CRE by appropriate areas of each band. The results are expressed in units of terawatts (TW or 10^{12} W) and represent the net contribution of mixed-phase clouds to energy imbalances at each latitude. These heat fluxes modify equator-to-pole temperature gradients that drive atmospheric circulations so the TOA, ATM, and SFC panels of Table 4 represent the impact of mixed-phase clouds on net, atmospheric, and oceanic heat transports, respectively. A positive (negative) heat flux denotes a net gain (loss) of energy in the relevant region.

The top panel of Table 4 demonstrates that on the annual mean mixed-phase clouds enhance net poleward heat transport in both hemispheres by cooling high latitudes ($40-60^\circ$) more effectively than lower latitudes relative to clear-sky conditions. This effect is strongest in the Southern Hemisphere where mixed-phase clouds cool the Southern Ocean 4 times more than the equator, resulting in a stronger poleward circulation in local summer months. In winter the impact of mixed-phase clouds reverses owing to their warming influence at high latitudes when solar insolation is weaker and implying that mixed-phase clouds moderate poleward heat transport in local winter. Similar but muted effects are observed in the Northern Hemisphere where the seasonal amplitude of net CRE is about half that over the Southern Ocean.

This integrated top-of-atmosphere perspective, however, masks important competing impacts of mixed-phase clouds on atmospheric and oceanic heat transport. Within the atmosphere, mixed-phase clouds exert a decidedly positive heat flux in the tropics and a negative heat flux poleward of 60° in all seasons. This augments existing energy imbalances and implies that mixed-phase clouds significantly enhance the atmospheric heat transport from tropics to poles. These impacts are particularly strong in the summer hemisphere as shown in the center panel of Table 4.

The implied enhancement of atmospheric poleward heat transport is partially compensated by an opposite effect in the ocean surface. The stronger reduction of heat fluxes into the tropical oceans relative to higher latitudes especially during the winter months partially reduces the natural zonal gradient in sea surface

Table 4. Monthly Mean Heat Flux From Mixed-Phase Clouds, Binned in 20° Latitude Bands From 80°S to 80°N^a

		Heat flux from mixed-phase clouds (TW)														
		Jan	Feb	Mar	Apr	May	Jun	Jul	Aug	Sep	Oct	Nov	Dec	Ann		
TOA	80N	38	23	-35	-118	-305	-401	-298	-225	-91	46	69	49	-104	80N	
	40N	34	-106	-328	-510	-585	-546	-424	-302	-206	-98	18	80	-248	40N	
	Eq	-65	-164	-169	-249	-261	-251	-240	-194	-150	-92	-40	-21	-158	Eq	
	40S	-113	-119	-118	-126	-165	-191	-236	-286	-205	-135	-120	-80	-158	40S	
	80S	-225	-234	-152	-97	-49	-35	-46	-68	-81	-141	-165	-159	-121	80S	
	Ann	-287	-253	-144	-73	-9	29	-14	-89	-224	-307	-351	-328	-171	Ann	
ATM	80N	-1073	-820	-464	-139	74	165	94	-102	-470	-840	-1156	-1168	-492	80N	
	40N	-524	-429	-149	4	51	45	33	16	-37	-121	-290	-436	-153	40N	
	Eq	-129	-139	-100	-106	-147	-68	-23	-38	-149	-257	-204	-148	-126	Eq	
	40S	-229	-179	-101	0	134	256	278	233	98	-62	-175	-212	3	40S	
	80S	38	78	142	203	263	305	299	278	250	186	131	94	189	80S	
	Ann	211	193	239	314	414	490	567	628	573	455	338	269	391	Ann	
SFC	80N	513	522	447	357	228	162	145	138	189	253	339	425	310	80N	
	40N	266	278	226	204	163	123	90	90	137	192	276	274	193	40N	
	Eq	33	13	-85	-157	-205	-222	-247	-235	-197	-131	-53	29	-121	Eq	
	40S	-189	-210	-231	-215	-161	-135	-112	-112	-120	-132	-163	-167	-162	40S	
	80S	166	162	65	-12	-159	-333	-275	-187	58	303	272	197	22	80S	
	Ann	262	73	-228	-510	-718	-801	-702	-535	-304	-35	193	292	-251	Ann	
SFC	80N	-103	-242	-311	-453	-524	-556	-540	-473	-400	-278	-171	-115	-347	80N	
	40N	-324	-312	-357	-440	-579	-680	-803	-914	-778	-590	-458	-349	-549	40N	
	Eq	-739	-756	-599	-454	-277	-197	-192	-207	-271	-394	-504	-584	-431	Eq	
	40S	-553	-531	-370	-277	-173	-94	-105	-179	-361	-498	-627	-602	-364	40S	
	80S	-1107	-833	-379	18	279	387	341	133	-273	-709	-1103	-1197	-370	80S	
	Ann	-335	-220	82	219	212	180	145	128	83	11	-127	-268	9	Ann	

^aHeat flux, reported in units of Terawatts (TW or 10^{12} W), is computed at the top of atmosphere (TOA), surface (SFC), and in atmosphere (ATM). A positive (negative) heat flux represents a net gain (loss) of energy at a given atmospheric level. All data are from R05 FLXHR-LIDAR, 2007–2010.

temperature relative to clear conditions. When coupled with known ocean circulation patterns, this suggests that mixed-phase clouds reduce poleward heat transport in the oceans but, in contrast to the atmospheric heat transport, these effects are maximum in the winter hemisphere. It will be demonstrated below that these offsetting effects of mixed-phase clouds find their origins in differences in the distribution of precipitating and nonprecipitating mixed-phase clouds between the tropics and higher latitudes.

6. Mixed-Phase Cloud Regimes

It is important to note that the definition adopted here for mixed-phase clouds is comprehensive and includes all clouds in which both phases exist. The sensors aboard CloudSat and CALIPSO are sensitive to a wide range of mixed-phase clouds, from the traditional definition of nonprecipitating mixed-phase clouds consisting of a liquid layer at the top and ice precipitating from below to stratiform and convective precipitation that consist of snow aloft, rain at low levels, and varying mixtures of liquid and ice cloud water throughout. The 2B-FLXHR-LIDAR product has the unique capability to quantify the contributions of each of these types of mixed-phase clouds to global CRE, as shown in Figure 11 (left column). Precipitating or nonprecipitating

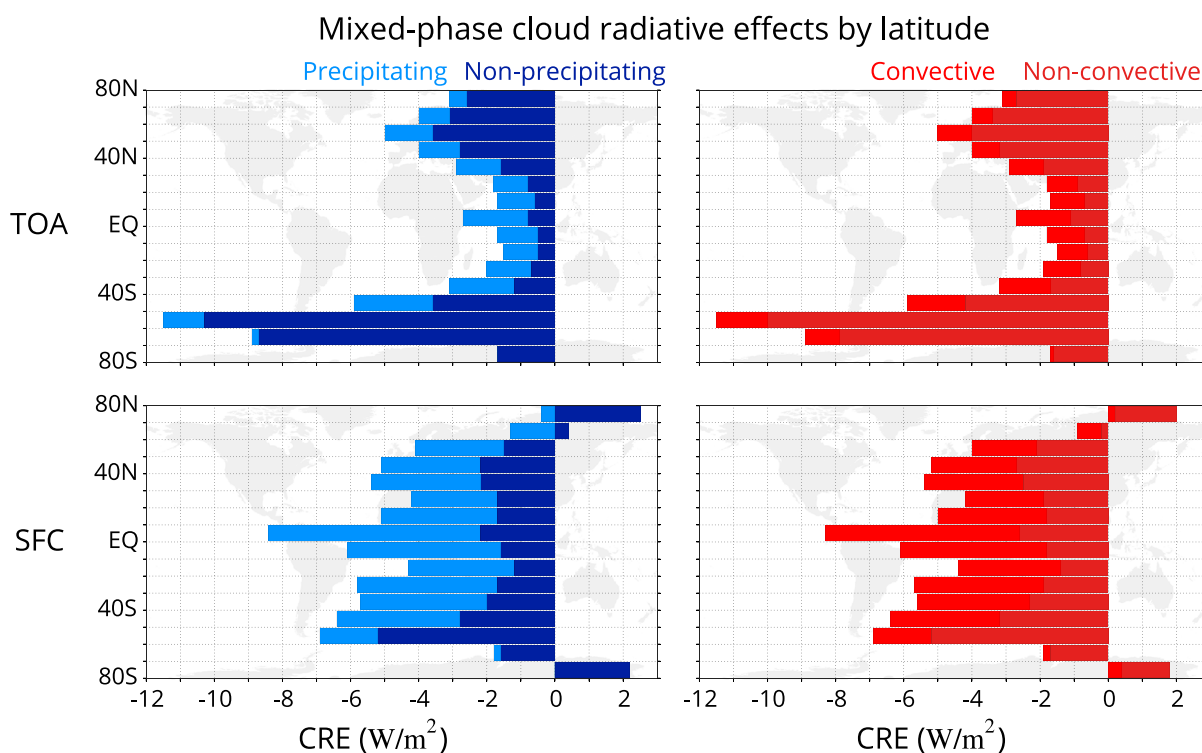


Figure 11. Annual mean net radiative effects from mixed-phase clouds, binned into 10° latitude bands. Cloud radiative effects at the TOA and surface are stratified by (left column) convective/nonconvective clouds and (right column) precipitating/nonprecipitating clouds. All data are from R05 FLXHR-LIDAR, 2007–2010.

scenes are identified for each profile using CloudSat's 2C-PRECIP-COLUMN, which performs retrievals of precipitation occurrence and intensity based on near-surface radar reflectivity and estimates of path-integrated attenuation [Haynes *et al.*, 2009]. Nonprecipitating mixed-phase clouds account for over 65% of the total radiative impact at the TOA. The impact of nonprecipitating clouds is considerably greater at higher latitudes and about twice as strong in the Southern Hemisphere than the Northern Hemisphere. At the surface, however, precipitating clouds have larger radiative effects than nonprecipitating mixed-phase clouds in the tropics. Poleward of 70° , however, precipitating clouds have a negligible radiative effect, while nonprecipitating clouds exert a warming effect in excess of 2 W m^{-2} .

Vertically resolved measurements from CloudSat and CALIPSO also have the capability to distinguish stratiform mixed-phase clouds from their more convective counterparts whose origins can be traced to more turbulent mixing in stronger updrafts. While the majority of mixed-phase clouds at higher latitudes are nonconvective in nature, tropical mixed-phase clouds are predominantly associated with convection. Figure 11 (right column) shows the partitioning of mixed-phase cloud radiative effects by their contributions from convective and nonconvective regimes. Convective clouds are defined in this study as those identified by the 2B-CLDCLASS-LIDAR data set as nimbostratus or deep convection cloud type classifications, while all other clouds are identified as nonconvective. Based on these criteria, the global annual mean radiative effect of convective mixed-phase clouds at TOA is -0.9 W m^{-2} or 28% of the total. Similar to precipitating mixed-phase clouds, however, convective clouds exert a greater radiative effect at the surface than the TOA. Convective mixed-phase CRE at the surface is -2.7 W m^{-2} and accounts for 59% of the total. It follows that mixed-phase clouds observed in the tropics are primarily convective systems that are raining, whereas those nearer the poles are generally nonconvective and nonprecipitating.

7. Discussion and Conclusion

The partitioning of water between its liquid and ice phases plays an important yet not fully understood role in the global energy budget. Mixed-phase clouds are of particular interest given their strong and variable impact on the TOA and surface energy budget at higher latitudes. While previous studies have assessed

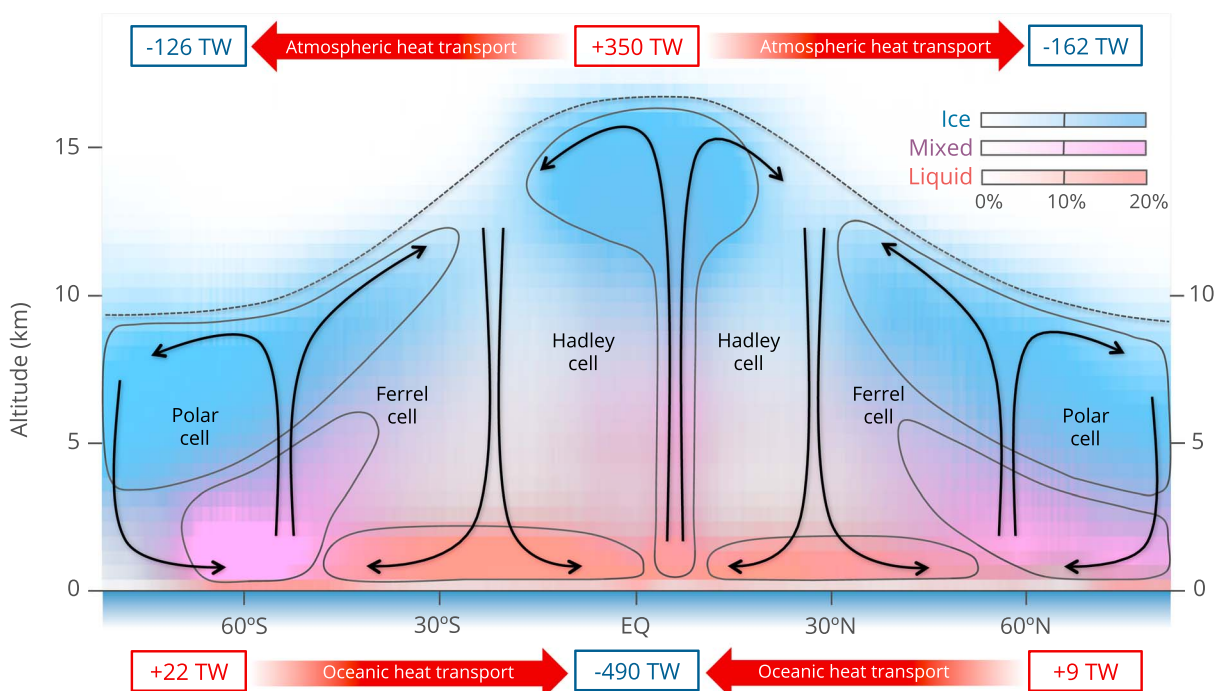


Figure 12. Conceptual illustration of the location of mixed-phase clouds and their influence on global heat transport. Boxed values indicate the contribution of annual heat flux from mixed-phase clouds within the atmosphere and at the surface. Color shading indicates the observed cloud occurrence of liquid (red), ice (blue), and mixed-phase (purple) clouds using cloud phase classification data from 2B-CLDCLASS-LIDAR, 2007–2010. For illustrative purposes, black arrows indicate the general structure of large-scale atmospheric circulations and gray outlines indicate the boundaries of idealized cloud regimes.

the radiative effects from mixed-phase clouds, a lack of adequate observations of cloud vertical structure may limit the fidelity of these estimates. We present a new assessment of the global radiative effect of mixed-phase clouds using the fifth release CloudSat fluxes and heating rates (R05 2B-FLXHR-LIDAR) product. The R05 2B-FLXHR-LIDAR product, which combines collocated CloudSat, CALIPSO, and MODIS observations to compute vertically resolved profiles of shortwave and longwave radiative fluxes, features an improved representation of cloud phase over previous versions. Our approach employs a relatively straightforward classification of cloud profiles into liquid, ice, mixed-phase, and multilayered scenes using CloudSat and CALIPSO observations. The combination of CloudSat and CALIPSO provides vertically resolved cloud measurements critical to filling in existing gaps in cloud partitioning and better constraining global estimates of cloud radiative effects. Simply partitioning these observations by cloud phase avoids some of the inherent ambiguity associated with more complicated cloud classifications, relates more closely to the raw observations, and can more easily be compared to prognostic fields in models.

While this study documents global estimates of cloud radiative effect for all water phases, mixed-phase clouds are of particular interest. Mixed-phase clouds are observed most frequently at higher latitudes, where they are efficient at reflecting solar radiation back to space and exert a negative radiative effect at the TOA. At the surface, however, the strongest mixed-phase CRE is from precipitating convective clouds in the tropics where SW cooling dominates LW heating. Over ice-covered surfaces such as Greenland and West Antarctica where SW effects are small, LW heating from nonprecipitating mixed-phase clouds dominates resulting in a strong positive net radiative effect at the surface. Mixed-phase clouds are found to exert a global net cloud radiative effect of -3.4 W m^{-2} , with contributions of -8.1 W m^{-2} and 4.7 W m^{-2} in the SW and LW, respectively. Interestingly, mixed-phase clouds contribute over 20% of the total cloud radiative effect despite making up only 10% of the total cloud occurrence. When compared with the effects of liquid clouds (-11.8 W m^{-2}), ice clouds (3.5 W m^{-2}), and multilayered clouds with distinct layers of liquid and ice (-5.4 W m^{-2}), these results confirm that accurate representation of mixed-phase clouds is essential for quantifying cloud feedbacks in future climate scenarios. This is particularly apparent over the Southern Ocean, where mixed-phase clouds are found to account for more than 35% of the net reduction of absorbed SW radiation at the surface in the

local summer. Recent modeling studies have suggested that this can have important implications for atmospheric and oceanic circulations on global scales [Komurcu *et al.*, 2014; Cesana *et al.*, 2015]

This is illustrated conceptually in Figure 12 that presents a schematic showing the locations where mixed-phase clouds occur and their influence on large-scale circulations. The annual occurrences of mixed-phase clouds (purple), liquid only clouds (red), and ice only clouds (blue) are computed globally at 480 m vertical resolution based on the 2B-CLDCLASS-LIDAR cloud phase classification data from 2007 to 2010. For illustrative purposes, gray outlines indicate the boundaries of idealized cloud structures and the canonical atmospheric flow patterns from the Hadley, Ferrel, and Polar cells are indicated by black arrows for context [Wallace and Hobbs, 2006]. Areas of rising air loosely coincide with regions of increased cloudiness, especially convective mixed-phase clouds. As previously shown in Figure 4, mixed-phase cloud systems are indeed most frequent over the tropics and upper midlatitudes. Multilayered clouds are also quite common over these regions and, most notably in the tropics, where high cirrus is often observed above liquid or mixed-phase convective cloud systems. In regions of large-scale subsidence, liquid clouds dominate but mixed-phase clouds are frequently observed at polar latitudes.

Results from this study provide key observational benchmarks which can be used to improve climate model simulations of cloud radiative effects. It is important to note, however, that several important sources of uncertainty remain in these estimates. Most notably, it remains difficult to accurately partition water between its liquid and ice phases in layers where they coexist. Diurnal sampling limitations and assumed surface reflection characteristics may also influence the results. The approximate magnitude of these uncertainties has been quantified, to the extent possible, through cloud regime-specific comparisons against CERES TOA fluxes in Table 2. These comparisons suggest that the resulting uncertainties in the annual mean radiative effects of mixed-phase clouds presented here are 10–15%.

Overall, mixed-phase clouds are found to heat the tropical atmosphere by increasing the greenhouse effect and cool the polar atmosphere by enhancing LW emission to the surface. This suggests that mixed-phase clouds increase the equator-to-pole temperature gradient and act to reinforce large-scale poleward atmospheric heat transport. The opposite is true in the oceans where convective mixed-phase clouds cool the tropical ocean, but nonprecipitating nonconvective mixed-phase clouds slightly warm the surface in the Arctic and Antarctic. This weakens the equator-to-pole temperature gradient in the ocean and, when combined with ocean circulation patterns, likely reduces oceanic poleward heat transport in the annual mean. These results support recent modeling studies that have demonstrated the importance of cloud phase partitioning for accurately representing large-scale atmospheric and oceanic circulations [Kay *et al.*, 2016; Storelvmo *et al.*, 2008].

Acknowledgments

The authors gratefully acknowledge Kristof van Tricht for his contributions in the development of the fifth release CloudSat fluxes and heating rates data set. All CloudSat data were acquired through the CloudSat Data Processing Center (DPC) and can be accessed at <http://www.cloudsat.cira.colostate.edu>. The authors thank Phil Partain and the staff at the DPC for their assistance in data processing. This research was supported by NASA CloudSat/CALIPSO Science Team grant NNX13AQ32G. The preliminary version of the R05 FLXHR-LIDAR data presented here was processed by request at the DPC.

References

- Allan, R. P. (2011), Combining satellite data and models to estimate cloud radiative effect at the surface and in the atmosphere, *Meteorol. Appl.*, *18*(3), 324–333, doi:10.1002/met.285.
- Atkinson, J. D., B. J. Murray, M. T. Woodhouse, T. F. Whale, K. J. Baustian, K. S. Carslaw, S. Dobbie, D. O'Sullivan, and T. L. Malkin (2013), The importance of feldspar for ice nucleation by mineral dust in mixed-phase clouds, *Nature*, *498*(7454), 355–358, doi:10.1038/nature12278.
- Bony, S., R. Colman, and V. Kattsov (2006), How well do we understand and evaluate climate change feedback processes?, *J. Clim.*, *19*, 3445–3482.
- Cesana, G., J. E. Kay, H. Chepfer, J. M. English, and G. De Boer (2012), Ubiquitous low-level liquid-containing Arctic clouds: New observations and climate model constraints from CALIPSO-GOCCP, *Geophys. Res. Lett.*, *39*, L20804, doi:10.1029/2012GL053385.
- Cesana, G., D. E. Waliser, X. Jiang, and J. L. F. Li (2015), Multimodel evaluation of cloud phase transition using satellite and reanalysis data, *J. Geophys. Res. Atmos.*, *120*, 7871–7892, doi:10.1002/2014JD022932.
- Chepfer, H., D. Cesana, D. Winker, B. Getzewich, M. Vaughan, and Z. Liu (2013), Comparison of two different cloud climatologies derived from CALIOP-attenuated backscattered measurements (Level 1): The CALIPSO-ST and the CALIPSO-GOCCP, *J. Atmos. Oceanic Technol.*, *30*(4), 725–744, doi:10.1175/JTECH-D-12-00057.1.
- Christensen, M. W., G. L. Stephens, and M. D. Lebsock (2013), Exposing biases in retrieved low cloud properties from CloudSat: A guide for evaluating observations and climate data, *J. Geophys. Res. Atmos.*, *118*, 12,120–12,131, doi:10.1002/2013JD020224.
- Christensen, M. W., A. Behrang, T. L'Ecuyer, N. B. Wood, M. D. Lebsock, and G. L. Stephens (2016), Arctic observation and reanalysis integrated system: A new data product for validation and climate study, *Bull. Am. Meteorol. Soc.*, *97*, 907–915, doi:10.1175/BAMS-D-14-00273.1.
- Deng, M., G. G. Mace, Z. Wang, and R. Paul Lawson (2013), Evaluation of several A-Train ice cloud retrieval products with in situ measurements collected during the SPARTICUS campaign, *J. Appl. Meteorol. Climatol.*, *52*(4), 1014–1030, doi:10.1175/JAMC-D-12-054.1.
- Flato, G., *et al.* (2013), Evaluation of climate models, in *Climate Change 2013: The Physical Science Basis. Contribution of Working Group I to the Fifth Assessment Report of the Intergovernmental Panel on Climate Change*, edited by T. F. Stocker *et al.*, pp. 741–866, Cambridge Univ. Press, Cambridge, U. K., and New York, doi:10.1017/CBO9781107415324.
- Forbes, R. M., and M. Ahlgrimm (2014), On the representation of high-latitude boundary layer mixed-phase cloud in the ECMWF global model, *Mon. Weather Rev.*, *142*(9), 3425–3446, doi:10.1175/MWR-D-13-00325.1.

- Fu, Q., and K. N. Liou (1993), Parameterization of the radiative properties of cirrus clouds, *J. Atmos. Sci.*, *50*, 2008–2025, doi:10.1175/1520-0469(1993)050<2008:POTRPO>2.0.CO;2.
- Gettelman, A., H. Morrison, and S. J. Ghan (2007), A new two-moment bulk stratiform cloud microphysics scheme in the NCAR Community Atmosphere Model (CAM3). Part II: Single-column and global results, *J. Clim.*, *21*, 3660–3679, doi:10.1175/2008JCLI2116.
- Haynes, J. M., T. S. L'Ecuyer, G. L. Stephens, S. D. Miller, C. Mitrescu, N. B. Wood, and S. Tanelli (2009), Rainfall retrieval over the ocean with spaceborne W-band radar, *J. Geophys. Res.*, *114*, D00A22, doi:10.1029/2008JD009973.
- Henderson, D. S., and T. S. L'Ecuyer (2011), Level 2B fluxes and heating rates and 2B fluxes and heating rates w/ lidar process description and interface control document, Tech. Rep. D, CloudSat Algorithm Process Description Documents.
- Henderson, D. S., T. L'Ecuyer, G. Stephens, P. Partain, and M. Sekiguchi (2013), A multisensor perspective on the radiative impacts of clouds and aerosols, *J. Appl. Meteorol. Climatol.*, *52*(4), 853–871, doi:10.1175/JAMC-D-12-025.1.
- Hogan, R. J., P. N. Francis, H. Flentje, A. J. Illingworth, M. Quante, and J. Pelon (2003), Characteristics of mixed phase clouds. Part I: Lidar, radar and aircraft observations from CLARE '98, *Q. J. R. Meteorol. Soc.*, *129*, 2089–2116, doi:10.1256/qj.01.208.
- Hogan, R. J., M. D. Behera, E. J. O'Connor, and A. J. Illingworth (2004), Estimate of the global distribution of stratiform supercooled liquid water clouds using the LITE lidar, *J. Geophys. Res.*, *31*, L05106, doi:10.1029/2003GL018977.
- Hu, Y., S. Rodier, K. M. Xu, W. Sun, J. Huang, B. Lin, P. Zhai, and D. Josset (2010), Occurrence, liquid water content, and fraction of supercooled water clouds from combined CALIOP/IIR/MODIS measurements, *J. Geophys. Res.*, *115*, D00H34, doi:10.1029/2009JD012384.
- Kato, S., S. Sun-Mack, W. F. Miller, F. G. Rose, Y. Chen, P. Minnis, and B. A. Wielicki (2010), Relationships among cloud occurrence frequency, overlap, and effective thickness derived from CALIPSO and CloudSat merged cloud vertical profiles, *J. Geophys. Res.*, *115*, D00H28, doi:10.1029/2009JD012277.
- Kay, J. E., L. Bourdages, N. B. Miller, A. Morrison, V. Yettella, H. Chepfer, and B. Eaton (2016), Evaluating and improving cloud phase in the Community Atmosphere Model version 5 using spaceborne lidar observations, *J. Geophys. Res. Atmos.*, *121*, 4162–4176, doi:10.1002/2015JD024699.
- Kiehl, J. T., J. J. Hack, and B. P. Briegleb (1994), The simulated Earth radiation budget of the National Center for Atmospheric Research community climate model CCM2 and comparisons with the Earth Radiation Budget Experiment (ERBE), *J. Geophys. Res.*, *99*(D10), 20,815–20,827, doi:10.1029/94JD00941.
- Komurcu, M., T. Storelvmo, I. Tan, U. Lohmann, Y. Yun, J. E. Penner, Y. Wang, X. Liu, and T. Takemura (2014), Intercomparison of the cloud water phase among global climate models, *J. Geophys. Res. Atmos.*, *119*, 3372–3400, doi:10.1002/2013JD021119.
- L'Ecuyer, T. S., N. B. Wood, T. Haladay, G. L. Stephens, and P. W. Stackhouse (2008), Impact of clouds on atmospheric heating based on the R04 CloudSat fluxes and heating rates data set, *J. Geophys. Res.*, *113*, D00A15, doi:10.1029/2008JD009951.
- L'Ecuyer, T. S., et al. (2015), The observed state of the energy budget in the early twenty-first century, *J. Clim.*, *28*(21), 8319–8346, doi:10.1175/JCLI-D-14-00556.1.
- Loeb, N. G., J. M. Lyman, G. C. Johnson, R. P. Allan, D. R. Doelling, T. Wong, B. J. Soden, and G. L. Stephens (2012), Observed changes in top-of-the-atmosphere radiation and upper-ocean heating consistent within uncertainty, *Nat. Geosci.*, *5*(2), 110–113, doi:10.1038/ngeo1375.
- Lü, Q., J. Li, T. Wang, and J. Huang (2015), Cloud radiative forcing induced by layered clouds and associated impact on the atmospheric heating rate, *J. Meteorol. Res.*, *29*(5), 779–792, doi:10.1007/s13351-015-5078-7.
- Mccoy, D. T., D. L. Hartmann, M. D. Zelinka, P. Ceppi, and D. P. Grosvenor (2015), Mixed-phase cloud physics and Southern Ocean cloud feedback in climate models, *J. Geophys. Res. Atmos.*, *120*, 9539–9554, doi:10.1002/2015JD023603.
- McCoy, D. T., S. M. Burrows, R. Wood, D. P. Grosvenor, S. M. Elliott, P.-L. Ma, P. J. Rasch, and D. L. Hartmann (2015), Natural aerosols explain seasonal and spatial patterns of Southern Ocean cloud albedo, *Sci. Adv.*, *1*(6), e1500157, doi:10.1126/sciadv.1500157.
- McIlhatten, E. A., T. L'Ecuyer, and N. Miller (2017), Too much powder? Observational evidence for a physical mechanism behind model supercooled liquid cloud biases, *J. Clim.*, in press.
- Miller, S. D., Y.-J. Noh, and A. K. Heidinger (2014), Liquid-top mixed-phase cloud detection from shortwave-infrared satellite radiometer observations: A physical basis, *J. Geophys. Res. Atmos.*, *119*, 8245–8267, doi:10.1002/2013JD021262.
- Morrison, H., et al. (2011), Intercomparison of cloud model simulations of Arctic mixed-phase boundary layer clouds observed during SHEBA/FIRE-ACE, *J. Adv. Model. Earth Syst.*, *3*, M06003, doi:10.1029/2011MS000066.
- Murray, E. J., B. J. Murray, and V. Sivakumar (2013), Ice nucleation by particles immersed in supercooled cloud droplets, *Chem. Soc. Rev.*, *42*(24), 9571–9572.
- Prenni, A. J., J. Y. Harrington, M. Tjernstöm, P. J. DeMott, A. Avramov, C. N. Long, S. M. Kreidenweis, P. Q. Olsson, and J. Verlinde (2007), Can ice-nucleating aerosols affect arctic seasonal climate?, *Bull. Am. Meteorol. Soc.*, *88*(4), 541–550, doi:10.1175/BAMS-88-4-541.
- Pruppacher, H. R., J. D. Klett, and P. K. Wang (1998), Microphysics of clouds and precipitation, *Aerosol Sci. Technol.*, *28*(4), 381–382.
- Randall, D. A., et al. (2007), Climate models and their evaluation, in *Climate Change 2007: The Physical Science Basis. Contribution of Working Group I to the Fourth Assessment Report of the IPCC (FAR)*, edited by S. Solomon et al., pp. 589–662, Cambridge Univ. Press, Cambridge, U. K., and New York.
- Rauber, R. M., and A. Tokay (1991), An explanation for the existence of supercooled water at the top of cold clouds, *J. Atmos. Sci.*, *48*, 1005–1023, doi:10.1175/1520-0469(1991)048<1005:AEFTEO>2.0.CO;2.
- Ritter, B., and J.-F. Geleyn (1992), A comprehensive radiation scheme for numerical weather prediction models with potential applications in climate simulations, *Mon. Weather Rev.*, *120*(2), 303–325, doi:10.1175/1520-0493(1992)120<0303:ACRSFN>2.0.CO;2.
- Sassen, K., and Z. Wang (2012), The clouds of the middle troposphere: Composition, radiative impact, and global distribution, *Surv. Geophys.*, *33*(3–4), 677–691, doi:10.1007/s10712-011-9163-x.
- Slingo, A. (1989), A GCM parameterization for the shortwave radiative properties of water clouds, *J. Atmos. Sci.*, *46*, 1419–1427, doi:10.1175/1520-0469(1989)046<1419:AGPFTS>2.0.CO;2.
- Soden, B., and I. Held (2006), An assessment of climate feedbacks in coupled ocean-atmosphere models, *J. Clim.*, *19*(23), 3354–3360, doi:10.1175/JCLI9028.1.
- Stephens, G. L., and T. L'Ecuyer (2015), The Earth's energy balance, *Atmos. Res.*, *166*, 195–203, doi:10.1016/j.atmosres.2015.06.024.
- Storelvmo, T., J. E. Kristjánsson, and U. Lohmann (2008), Aerosol influence on mixed-phase clouds in CAM-Oslo, *J. Atmos. Sci.*, *65*(10), 3214–3230, doi:10.1175/2008JAS2430.1.
- Tsushima, Y., S. Emori, T. Ogura, M. Kimoto, M. J. Webb, K. D. Williams, M. A. Ringer, B. J. Soden, B. Li, and N. Andronova (2006), Importance of the mixed-phase cloud distribution in the control climate for assessing the response of clouds to carbon dioxide increase: A multi-model study, *Clim. Dyn.*, *27*(2–3), 113–126, doi:10.1007/s00382-006-0127-7.
- van Tricht, K., S. Lhermitte, J. T. M. Lenaerts, I. V. Gorodetskaya, T. S. L'Ecuyer, B. Noël, M. R. van den Broeke, D. D. Turner, and N. P. M. van Lipzig (2016), Clouds enhance Greenland ice sheet meltwater runoff, *Nat. Commun.*, *7*, 10266, doi:10.1038/ncomms10266.
- Verlinde, J., et al. (2007), The mixed-phase arctic cloud experiment, *Bull. Am. Meteorol. Soc.*, *88*(2), 205–221, doi:10.1175/BAMS-88-2-205.

- Vial, J., J. L. Dufresne, and S. Bony (2013), On the interpretation of inter-model spread in CMIP5 climate sensitivity estimates, *Clim. Dyn.*, *41*(11–12), 3339–3362, doi:10.1007/s00382-013-1725-9.
- Wallace, J. M., and P. V. Hobbs (2006), *Atmospheric Science*, pp. 419–465, Elsevier, doi:10.1016/B978-0-12-732951-2.50015-6.
- Wild, M., D. Folini, M. Z. Hakuba, C. Schar, S. I. Seneviratne, S. Kato, D. Rutan, C. Ammann, E. F. Wood, and G. König-Langlo (2014), The energy balance over land and oceans: An assessment based on direct observations and CMIP5 climate models, *Clim. Dyn.*, *44*, 3393–3429, doi:10.1007/s00382-014-2430-z.
- Zatko, M. C., and S. G. Warren (2015), East Antarctic sea ice in spring: Spectral albedo of snow, nilas, frost flowers and slush, and light-absorbing impurities in snow, *Ann. Glaciol.*, *56*(69), 53–64, doi:10.3189/2015AoG69A574.
- Zelinka, M. D., S. A. Klein, K. E. Taylor, T. Andrews, M. J. Webb, J. M. Gregory, and P. M. Forster (2013), Contributions of different cloud types to feedbacks and rapid adjustments in CMIP5, *J. Clim.*, *26*(14), 5007–5027, doi:10.1175/JCLI-D-12-00555.1.
- Zhang, Y., W. B. Rossow, A. A. Lacis, V. Oinas, and M. I. Mishchenko (2004), Calculation of radiative fluxes from the surface to top of atmosphere based on ISCCP and other global data sets: Refinements of the radiative transfer model and the input data, *J. Geophys. Res.*, *109*, D19105, doi:10.1029/2003JD004457.